AN OVERVIEW OF THE FUNDAMENTAL AERODYNAMICS BRANCH'S RESEARCH ACTIVITIES IN WING LEADING-EDGE VORTEX FLOWS AT SUPERSONIC SPEEDS

David S. Miller, Richard M. Wood, and Peter F. Covell
NASA Langley Research Center
Hampton, Virginia

SUMMARY

For the past 3 years, a research program pertaining to the study of wing leading-edge vortices at supersonic speeds has been conducted in the Fundamental Aerodynamics Branch of the High-Speed Aerodynamics Division at the Langley Research Center. The purpose of the research is to provide an understanding of the factors governing the formation and the control of wing leading-edge vortices and to evaluate the use of these vortices for improving supersonic aerodynamic performance. The studies include both experimental and theoretical investigations and focus primarily on planform, thickness and camber effects for delta wings. This paper will present an overview of this research activity.

INTRODUCTION

During the last 20 years, aerodynamicists have attempted to design aircraft wings for efficient supersonic flight using attached-flow concepts. For cruise levels of lift, linearized-theory wing-design methods (refs. 1 and 2) have successfully produced optimum twisted and cambered wings. Because of the early success of these methods, the methods have been continuously modified and refined to include the effects of component-on-wing interference (ref. 3), real-flow constraints (ref. 4), and attainable leading-edge thrust (ref. 5). Example applications of this low level-of-lift wing-design technology can be found in references 6 through 8.

For maneuver levels of lift at supersonic speeds, basically two approaches are available for the design of wings. One approach is to provide an attached-flow, controlled expansion around the wing leading edge and on the upper surface (refs. 9 and 10). This attached-flow approach for producing efficient high lift depends on the ability to accelerate the flow around the leading edge to supercritical conditions on the upper surface and then decelerate the flow without causing separation or producing strong shocks. This concept has been experimentally verified, and a summary of the investigation is given in reference 11. The second approach for obtaining efficient high-lift wings uses a controlled, separated, leading-edge vortex flow which not only produces vortex lift, but when the vortex is properly located on a deflected leading-edge, also produces significant levels of effective leading-

edge thrust. Investigations at subsonic and transonic speeds (refs. 12 to 16) of the fundamental vortex behavior on the leeward surface of wings have led to the design of several unique and novel leading-edge devices (refs. 17 to 21) commonly referred to as "vortex flaps." Also, to aid in the design of vortex flaps, several computer codes (refs. 22 to 24) with varying degrees of complexity are being developed to predict vortex location, strength, and effect on the wing. As summarized in reference 25, the development of this new wing-design technology has been extensive but has been confined mainly to subsonic and transonic flows.

In 1982, a research effort was begun to explore the fundamental characteristics of wing leading-edge vortex flows at supersonic speeds. A review of the literature indicated that various aspects of the problem had been previously explored; however, there did not exist a complete and systematic set of experimental data from which one could determine the most basic effects such as Mach number, planform, thickness and camber. To provide this information, an experimental program was formulated first and closely followed by a complementary theoretical effort. This paper will present an overview of the experimental and theoretical programs. Following the overview, a discussion of aerodynamic performance is presented. In this discussion, a comparison is made between wings designed for optimum camber, wings with conventional leading-edge flaps, and wings with conical vortex flaps.

NOMENCLATURE

C_D drag coefficient

ΔC_D incremental change in drag coefficient from the minimum drag of a flat wing

C_L lift coefficient

C_{N_v} vortex induced normal-force coefficient

C_p pressure coefficient

C_{p_v} vacuum pressure coefficient

L model length

M Mach number

M_N component of Mach number normal to wing leading edge = $M \cos \Lambda (1 + \sin^2 \alpha \tan^2 \Lambda)^{1/2}$

X longitudinal distance measured from model origin

Y spanwise distance measured from model centerline

Y_{max} maximum spanwise model dimension

α angle of attack, deg

α_N angle of attack normal to wing leading edge = $\tan^{-1}(\tan\alpha/\cos\Lambda)$

β $\sqrt{M^2 - 1}$ and angle of yaw, deg

δ_f leading-edge-flap deflection angle measured streamwise, deg

Λ wing leading-edge-sweep angle, deg

η fraction of local wing semispan

DISCUSSION

An experimental-theoretical research effort is under way to investigate the fundamental characteristics of wing leading-edge vortex flows at supersonic speeds. In order to present a complete overview of the program, both completed, ongoing and planned investigations will be included in the following discussion.

Experimental Program

The primary objective of the experimental program is to obtain a complete and consistent set of data necessary to determine the effects of wing planform, thickness and camber on the characteristics of wing leading-edge vortex flows. To obtain a consistent set of data for the entire program, an effort was made to keep the wing planforms, flow conditions and types of data consistent throughout. The specific ingredients for consistency were established in the planform investigation which was the first part of the experimental research program.

Wing planform investigation. - Shown in figure 1 are planform sketches of the 4 wind tunnel models selected for testing. The models had leading-edge-sweep values ranging from 52.5° to 75°. In this initial test, it was desirable to minimize the effect of airfoil shape and thickness; therefore, the leading edge was made sharp (10° angle normal to leading edge located on lower surface) and the upper surface was made flat. Each model had a span of 12 in. and a spanwise row of 19 evenly spaced pressure orifices located approximately 1 in. forward of the trailing edge.

Previous experimental tests employed only a single type of flow-visualization data with or without pressure data to explain the vortex phenomena. However, as shown in figure 2, these experimental pressure data were obtained along with three types of flow-visualization data. As shown at the

top of the figure, both tuft and oil-flow photographs were used to examine the flow characteristics on the model surface. These two techniques give slightly different types of information. Both methods are used to determine surface flow direction by the alignment of the tufts or the streaking of the oil; however, the tufts tend to reflect the velocity direction at the edge of the boundary layer, and the direction of oil streaking is influenced not only by the surface velocity but also by the pressure distribution.

Only the vapor-screen flow-visualization technique provides flow-field information on the size, shape, and location of the vortex as shown in the lower right side of figure 2. The dark areas in the photographs are regions having less vapor than the light areas and thus, the dark areas correspond to the highly rotational vortex-flow regions in which the vapor particles have been displaced. Examples and discussion of these various types of data and their relationship with leading-edge vortex behavior are given in reference 26. Each model was tested at Mach numbers of 1.7, 2.0, 2.4 and 2.8 for angles of attack ranging from 0° to 20°.

In a previous study, Stanbrook and Squire (ref. 27) suggested that the flow conditions normal to the leading edge, specifically normal angle of attack (α_N) and normal Mach number (M_N), govern the type of flow which exists. Stanbrook and Squire initially reported that near $M_N = 1$ a boundary existed dividing the flow into two distinct regions: for $M_N < 1$ the flow was characterized by a leading edge, separated, rolled-up vortex-type flow and for $M_N > 1$ the flow was characterized by an attached flow with possible shock-induced separation. The classification into just two types of flow provided by the Stanbrook-Squire boundary was revised by Ganzer, Hoder and Szodruch (ref. 28); however, this latter effort was based on a single leading-edge-sweep angle of 73° and flow conditions of $M_N \geq 1$. A complete review of this work was presented by Szodruch and Peake (ref. 29). In the present planform study, four leading-edge-sweep values were used to examine the type of flow for conditions which lie above and below the $M_N = 1$ Stanbrook-Squire boundary.

Using primarily vapor-screen information, the types of flow observed in this test were divided into the seven categories as shown in figure 3. A detailed discussion of each of these flow types can be found in reference 26. In figure 4, all of the test data are summarized according to one of the seven flow types. The α_N - M_N space is clearly divided into regions where the flow type is indicated by the vapor-screen sketch placed in each region. As an added feature to provide additional information, the open symbols identify flows with shocks; the closed symbols identify shockless flows; the circular symbols identify flows with primary and secondary vortices; the square symbols identify flows containing separation bubbles; the diamond symbols identify flows with shock induced separation; and the triangle symbols identify flows with no separation. As shown by the solid triangles in the figure, the only flow conditions which produced shockless attached flows were angles of attack of zero ($\alpha_N = 0$); however, this occurs only because the next smallest angle of

attack in the test matrix was 4°. Because the two most effective types of separated flow being considered for aerodynamic performance enhancements are the shockless bubble and shockless vortex, it is interesting to note that these two types of flow occupy the majority of the region for M_N less than unity. Also above 20° normal angle of attack, the upper boundary of the region decreases towards $M_N = 0$ with increasing α_N.

Wing thickness investigation. - The experimental wing planform investigation was conducted with wind tunnel wing models designed to minimize the effects of airfoil shape and thickness; i.e., the leeward wing surface under investigation was made flat. However, calculated Euler code results, obtained by the method described in reference 30, are shown in figure 5 and indicate that the estimated effects of thickness can be significant. Mach number contours are shown for two delta wings each having 70° leading-edge-sweep angle but with different airfoil sections. One wing has a zero-thick airfoil section to represent a flat wing and the other wing has a 7-percent-thick circular-arc airfoil section. Although the calculations for both wings were made at exactly the same flow conditions of $M = 2.5$ and $\alpha = 18^0$, the Mach number contours indicate that the types of flow were completely different. The flow over the leeside of the zero-thick wing is characterized by a well-developed leading-edge vortex with a shock located on top of the vortex; the zero-thick wing flow conditions correspond to $M_N = 1.13$ and $\alpha_N = 44^0$ and, as shown in the $\alpha_N - M_N$ graphic, agree with the type of flow experimentally observed in the flat-wing planform study previously discussed. In contrast, flow over the leeside of the 7-percent circular-arc thick wing is characterized by a cross-flow shock with no signs of separation of any type. As indicated in figure 4, this type of flow would be expected to occur at a value of M_N greater than unity and a value of α_N less than 12°. Because the wing leading-edge local angle of attack is continuously varying along the span due to the nonconical geometry, it is not clear how to calculate the α_N and M_N values in order to apply the flow classification chart of figure 4. For this particular thick-wing example, reducing the wing angle of attack of 18° by 8° (which corresponds to one-half the value of the total thickness angle of the 7-percent parabolic arc at the leading edge) resulted in a $\alpha_N = 27^0$ and a $M_N = 0.95$ as shown for the thick wing location on the $\alpha_N - M_N$ chart in figure 5. This location corresponds to the boundary of several regions which all should have some type of separated flow. Obviously additional information is needed to understand the effects of thickness on the leeside-flow characteristics.

To provide a set of thick-wing data to compare with the flat-wing data, a set of eight wind tunnel wing models has been constructed. The models have delta planforms identical to the flat wings with leading-edge sweep angles of 52.5°, 60°, 67.5° and 75°. One set of models has 7-percent-thick circular-arc airfoil section and the other set of models has 7-percent-thick diamond airfoil sections (see fig. 6). Although both wing sets have the same thickness-to-chord ratio of 7 percent, their leading-edge thickness angles are considerably different. The circular-arc airfoil has a leading-edge thickness

half angle of approximately 8° and the diamond airfoil has a leading-edge thickness half angle of 4°. The test plans include oil flow, tuft and vapor screen flow-visualization data which will be correlated with the flat-wing flow-visualization data to identify thickness effects.

Wing-camber investigation. - The purpose of the wing-camber study was to experimentally determine the effects of wing leading-edge camber on both the aerodynamic forces and moments as well as the wing's leeside flow characteristics. The camber was represented by a deflected leading-edge flap on an otherwise uncambered wing having a flat upper surface. Two sets of delta-wing models were constructed. One set had a leading-edge-sweep angle of 67.5°, and the other set had a leading-edge-sweep angle of 75°. Each set had a leading-edge flap with its hinge line located at 70 percent of the local span; the leading-edge flap could be deflected down 0°, 5°, 10° or 15°. The flap deflection angle is measured streamwise. As shown in the photograph of figure 7, the models have a minimum-body balance housing which is conical back to approximately two-thirds of the model length at which point the body balance housing becomes cylindrical. As a result of this design, all model configurations tested had conical leeside surface geometries forward of the cylindrical portion of the body balance housing. For each of the two sets of wings, a removable fuselage forebody was constructed so that data could be obtained with and without fuselage forebody effects. The fuselage forebodies extended approximately 5 in. beyond the wing apex and had a fineness-ratio 2.5 circular-arc nose and a 2.0-in.-diameter cylindrical circular aft section.

Testing of the $\Lambda = 75^0$ wing with the fuselage forebody removed has been completed. Data were obtained for the same flow conditions as those of the planform study, i.e. Mach numbers from 1.5 to 2.8 and angles of attack from 0° to 20°. Figure 8 illustrates the behavior of the leeside flow characteristics at M = 1.7. Similar behavior was observed at the other Mach numbers. For the range of flap-deflection angles (δ_f) and angles of attack (α) tested, three distinctly different flow types were observed. The flow type is characterized by the existence, origin and location of the vortex and is denoted by the sketches on the figure. The sketch indicates the character of both the vortex and the associated surface pressure distribution. The shaded region corresponds to the situation in which the vortex originates at the wing leading edge and its primary influence is confined to the leading-edge flap; this is the ideal situation for the operation of a vortex flap. For angles of attack between 0° and 10°, the shaded region has both upper and lower boundaries. For a given angle of attack, the upper boundary denotes the flap-deflection angle above which the flow is attached on the flap but separates at the hinge line. For a given flap-deflection angle, the lower boundary denotes the angle of attack above which the vortex is no longer confined to the leading-edge flap but extends beyond the hinge line. There also exists a point where the upper and lower boundaries of the shaded region intersect. This point defines the maximum flap-deflection angle at which the leading-edge flap could be made to act as a vortex flap. It remains to be seen how the force and moment data

correlate with the leeside flow characteristics.

Because a definite interaction was observed between the hinge-line vortex and the leading-edge vortex, an experimental study of hinge-line separation is planned. As illustrated in figure 9, the hinge-line study will involve the testing of three hinge-line models mounted on a splitter plate. The models will have different leading-edge-sweep angles of 0°, 50°, and 70° and leading-edge flap deflection angles ranging from 0° to 40°. Each model will be instrumented so that pressure distributions can be measured both streamwise and normal to the hinge line. As indicated in the figure, flow field pressures will be measured using a flow survey pressure probe.

Theoretical Program

The objective of the theoretical program was to explore the use of computational methods for predicting the leading-edge vortex characteristics of wings at supersonic speeds. Two methods were examined. A modified linearized-theory method was found to adequately predict the flow characteristics of flat wings but was not adequate for predicting the flow over cambered wings. An Euler solution technique was found to adequately predict the general characteristics of both flat and cambered wings. The following discussion will briefly describe each method and highlight results obtained with each method.

Modified linearized-theory method. - A supersonic linearized-theory aerodynamic prediction method has been modified to account for both nonlinear attached-flow effects (primarily a windward surface phenomena) and nonlinear separated-flow effected (primarily a leeward surface phenomena) (ref. 31). The leading-edge separated flow is represented by a technique which uses the Polhamus suction analogy (ref. 32) to determine the leading-edge vortex-induced force and then modifies the upper surface attached-flow pressures to distribute this additional force over the wing upper surface. The vortex-induced force is distributed about a "vortex action point" located downstream of the wing leading edge. The location of the vortex action point is determined from an empirical relationship that is a function of angle of attack only. The method also limits the leeward surface pressures to values greater than those corresponding to vacuum conditions.

The ability of this modified linearized-theory method to predict wing vortex characteristics was evaluated for the series of flat delta wings used in the previously discussed experimental planform investigation. A detailed discussion of this evaluation is given in reference 26, and typical results are presented in figure 10. The results shown in the figure are for an uncambered delta wing with 75° of leading-edge sweep; the Mach numbers and angle of attack correspond to conditions which lie within the classical vortex region depicted in the upper portion of the figure. The vortex-induced normal-force coefficient, C_{N_V}, represents the vortex strength and the spanwise surface pressure distribution indicates both vortex strength and location. As

shown across the bottom of the figure, the agreement between theoretical and experimental results is sufficient for preliminary design applications of the modified linearized-theory method.

The method was next evaluated for wings with deflected leading-edge flaps. At the time of this evaluation, the experimental data had not been obtained on the conical wing-flap models described in the "Wing Camber Investigation" section of this paper; however, data from references 33 and 34 were sufficient to evaluate the method. A comparison of theoretical and experimental forces and surface pressures can be made from the results shown in figure 11. Although the pressure results were obtained at slightly different conditions than the force data, the flow characteristics which produced the force data at $C_L \approx 0.3$ closely correspond to the flow characteristics of the pressure distribution shown in the figure. Discrepancies between the experimental data and the computed results are found in both the drag polar and pressure distributions. The theoretical drag polars indicate that for values of lift-coefficient above 0.2 the wing with the 16° flap deflection produces less drag than the wing with zero flap deflection; however, the experimental data show that deflecting the leading-edge flap 16° resulted in a drag increase with respect to the wing with zero-flap deflection. An explanation for this discrepancy is clearly shown in the spanwise pressure distributions. The theoretical spanwise pressure distribution shows the presence of a small vortex its induced pressure acting on the leading-edge flap; theoretically this is the ideal situation for achieving performance benefits employing a vortex flap. However, the experimental pressures indicate both a small leading-edge vortex and a much larger hinge-line vortex. Because the hinge-line vortex induced pressures dominate and lie on the undeflected flat surface inboard of the hinge line, no drag reduction would be realized as a result of deflecting the leading-edge flap 16°.

From this discussion it is clear that the modified-linearized theory method is not capable of analyzing the flow over sharp leading-edge wings having deflected leading-edge flaps.

Euler code method. - Because the modified-linearized method failed to predict the leeside flow over delta wings with deflected leading-edge flaps, it was decided to explore the use of more complex codes such as Navier-Stokes and Euler codes. A number of researchers have applied Navier-Stokes codes and Euler codes to the calculation of wing leading-edge-vortex flows at supersonic speeds; and both methods have produced encouraging results for the flow over flat, uncambered wings (ref. 35). The Navier-Stokes equations model both the viscous and inviscid mechanisms and would be expected to provide the most accurate results. However, because Navier-Stokes methods have very high computational costs and because Euler methods have been shown to produce the general characteristics of vortex flows, it was decided to look first at the capabilities of Euler codes. In selecting a particular Euler code the choice ranged from large, complex 3-D, well-developed codes to a small, simple 2-D

conical code under development for the specific purpose of calculating wing leading-edge vortex flows. A code of the latter type, specifically the conical Euler code by Perez and Powell et al. (refs. 36 and 37), was selected because of the code developers' expressed interest in this particular problem.

A complete description of the code has been reported previously in reference 38 and only a brief description is presented herein. The basic solution technique employs a finite volume spatial discretization of the unsteady Euler equations in conservation form which is solved using a Runge-Kutta type method as discussed in reference 39. The bow shock is fitted, and both second and forth order damping are employed to capture internal shocks and yield smooth solutions. The grid is generated using a Joukowski transformation in which the zero-thick wing surface becomes a circle. For all calculations shown, the grid density consisted of 128 radial lines in the half plane and 128 points on each radial line. The wing is represented by zero-thick impermeable surface.

To compare with the Euler code solutions, eight cases were selected from the data obtained in the experimental program. The cases were selected to provide a large variety of wing leeside flow characteristics. In all eight cases, the geometry was a delta wing with 75° of leading-edge sweep. Four of the cases compare results for a flat wing, and four of the cases compare results for a wing with a deflected leading-edge flap.

The comparisons between experiment and theory include both flow-field and surface data. The calculated flow-field data consist of plots of the cross-flow velocity vectors and the measured flow-field data consist of vapor screen photographs. The flow-field data are presented in a plane perpendicular to the free-stream velocity vector. The calculated and measured surface data consist of spanwise pressure distributions.

Experimental and theoretical results for a flat wing at 12° angle of attack are shown in figures 12 and 13 for Mach numbers of 1.7 and 2.8, respectively. At both Mach numbers, the experimental and theoretical flow-field data show leading-edge separation which results in a well-developed primary vortex located above the leeside surface of the wing. The most notable difference between the theoretical and experimental results is the absence of the secondary vortex in the Euler results. This is found for all cases because the secondary vortex is a viscous phenomena which cannot be predicted by an inviscid Euler code. Otherwise, the agreement between the experimental and theoretical results is very good. Both results indicate the flattening and inboard movement of the primary vortex as Mach number is increased from 1.7 to 2.8. At Mach numbers of 1.7, the experimental and theoretical spanwise pressure distributions are in good agreement except for the influence of the secondary vortex. The experimental pressures show two pressure peaks, one near 60-percent span and another near 85-percent span; the theoretical pressure distributions show a single slightly higher pressure peak located at approximately the 70-percent span station. Although the higher Mach number

2.8 results of figure 12 still contain a secondary vortex, there is little or no influence of this secondary vortex on the surface pressure distribution. This observation seems to be typical, and it can be generally stated that effect of the secondary vortex on the wing upper surface pressures diminishes with increasing Mach number.

Results for a flat wing at 12° angle of attack and at 8° angle of yaw are shown in figures 14 and 15 for Mach numbers of 1.7 and 2.8, respectively. As seen in the figures, flow-field and surface-pressure data are shown for both the left side (y/y_{max} negative) and the right side (y/y_{max} positive) of the wing. For this yawed orientation, the left side of the wing has a windward leading edge and the right side has a leeward leading edge. Because vapor-screen photographs were not taken for the yawed wings, the only flow-field data shown are plots of the theoretically computed crossflow velocity vectors. In both figures 14 and 15, the asymmetry of the flow due to yaw is clearly shown in both the flow field and surface pressure data. For the low Mach number of 1.7, the cross-flow velocity contours show that leading-edge separation occurs on both the windward and leeward edges. The windward-edge separation develops into a separation bubble which lies close to the wing surface and the leeward-edge separation develops into a classical vortex. These two considerably different flow types result in different surface pressure distributions shown at the bottom of figure 14. The separation bubble results in a more negative pressure extending over a larger portion of the wing span as compared to the pressures resulting from the classical vortex. In figure 15, the higher Mach number 2.8 results indicate that the flow is attached on the windward edge and separated on the leeward edge. The attached flow produces a plateau-type pressure distribution over the outboard 75 percent of the left wing span; the pressure distribution on the right-wing span is typical of that produced by a classical vortex. For both Mach numbers, the Euler-code predicted pressures are in excellent agreement with the measured pressures.

Results from the experimental conical-wing-flap study indicated that four types of flow were observed to occur. The type of flow depends on the angle of attack and the wing leading-edge flap angle. To evaluate the ability of Euler code to predict the flow over the wings with deflected leading-edge flaps, four combinations of α and δ_f were selected to correspond to each of the four observed types of flow. These four α-δ_f combinations are shown in figure 16 and are labeled as points A, B, C, and D. The flow-field results and surface pressure distributions corresponding to points A, B, C, and D are shown in figures 17 to 20 respectively.

In figure 17, results are shown for $\alpha = 4^0$ and $\delta_f = 5^0$. According to the location of this condition on figure 16 (point A), the flow should be characterized by a classical leading-edge vortex. The experimental pressure distribution does indeed show a lower pressure region on the upper surface of the leading-edge flap, which could result from the presence of a weak vortex.

However, the experimental flow-field data do not show a vortex; this indicates that the vapor screen techniques may not be sensitive enough to detect weak vortex conditions or that condensation effects may have altered the flow conditions to delay vortex formation. Note also that neither the theoretical pressure distribution nor the theoretical flow-field data exhibit signs of a leading-edge vortex. These conflicting observations indicate that the characteristics of a weak vortex are very sensitive to the flow conditions.

In figure 18, results are shown for $\alpha = 12^0$ and $\delta_f = 5^0$. These results correspond to point B in figure 16. The experimental and theoretical results clearly show a primary vortex which originates at the wing leading edge and extends well inboard of the flap hinge line. The experimental and theoretical pressures are in good agreement and both reflect the presence of the primary vortex. The theoretical flow-field data unexpectedly indicate the presence of a secondary separation region lying on the leading-edge flap; this secondary separation is produced as the outboard flow passing under the primary vortex encounters the hinge line and separates. Although not clearly shown in the experimental flow-field data, both the experimental and theoretical pressure distributions exhibit the signs of this secondary separation.

Results for $\alpha = 4^0$ and $\delta_f = 15^0$ are shown in figure 19; these results correspond to point C on figure 16. The theoretical flow-field data show that a large flap deflection and small angle of attack produce two primary vortices. One of these vortices originates from the leading edge and lies on the lower surface of the leading-edge flap; this lower surface vortex cannot be seen in the experimental flow-field data because the light source is blocked by the leading-edge flap. The other primary vortex is produced when the attached flow on the flap upper surface separates at the flap hinge-line; this vortex lies inboard of the flap hinge line and is clearly visible in both the experimental and theoretical flow-field data. Although the vortex-induced pressures on the leeward wing surface are theoretically predicted slightly lower than those experimentally measured, the general agreement between theory and experiment is very good. The theoretically predicted pressure distribution shows the strong influence of the windward primary vortex as a reduced pressure region on the windward (lower) wing-flap surface; unfortunately, lower surface pressures were not measured and a comparison between experimental and theoretical pressures could not be made.

The fourth and final set of cambered delta-wing results are shown in figure 20. These results correspond to $\alpha = 12^0$ and $\delta_f = 15^0$ which is point D on figure 16. Both the experimental and the theoretical results indicate similar leeside flow characteristics. Both show leading-edge separation and hinge-line separation which result in two regions of vortex-type flow. The leading-edge vortex results in the most outboard suction pressure peak and the hinge-line vortex results in the largest suction pressure peak located slightly inboard of the hinge line. The major difference between the experimental and theoretical results is the extent of the leading-edge vortex. The

experimental results show a separation-bubble type vortex flow which extends over the entire length of the flap and produces the plateau type pressure distributions shown in the figure. The theoretical results also show a separation-bubble type vortex flow which begins at the wing leading edge and reattaches on the flap at approximately half way between the leading edge and the hinge line; in the theoretical distribution this flow reattachment produces the compression region between the two suction pressure peaks.

Aerodynamic Performance

In this section, the measured aerodynamic performance for a conical vortex-flap wing and the performance of a conventional attached-flow leading-edge flap wing are presented. These performance results are compared with each other and with a "practical performance goal" established from data measured on a series of optimum twisted and cambered wings.

Aerodynamic performance results for a vortex-flap wing are presented in figure 21. These results were obtained at M = 1.7 on the $\Lambda = 75^0$ delta wing with leading-edge flaps deflected 0°, 5°, 10° and 15°. Experimental values of drag-due-to-lift parameter are presented as a function of lift coefficient. For reference purposes, the linearized-theory 0-percent thrust and 100-percent thrust boundaries are also shown; these boundaries do not vary with lift coefficient. The data show that significant drag reductions can be achieved at supersonic speeds by the management of wing leading-edge vortices. Compared to the 5° flap-deflection data, which did not experience hinge-line separation, the data for the 10° and 15° leading-edge flap deflection show a loss in performance due to hinge-line separation. However, all flap deflections resulted in a drag reduction compared to the flat wing.

Aerodynamic performance results for a wing using a conventional attached-flow leading-edge flap were extracted from data obtained in the experimental study (ref. 40) depicted in figure 22. As indicated in the figure, the study involved testing four sets of flap planforms on a trapezoidal wing and two sets of flap planforms on a cranked wing. Both wings had aspect ratios of 1.75 and were mounted on a generic fuselage as shown in the photograph of figure 22. All leading-edge flap geometries were effective in reducing the flat-wing drag; however, the largest drag reductions were produced by the combination of flap A on the cranked wing. For this wing-flap combinations, experimental values of the drag-due-to-lift factor versus lift coefficient are shown in the lower left portion of the figure for flap deflection angles of 0°, 5° and 10°. The linearized-theory 0-percent thrust and 100-percent thrust boundaries are also shown. These data indicate that the lowest drag-due-to-lift is produced by scheduling the flap deflection angle with lift coefficient. As shown in the figure, the proper schedule would be $\delta_f = 0^0$ for lift coefficients below 0.1; $\delta_f = 5^0$ for lift coefficients between 0.1 and 0.4; and $\delta_f = 10^0$ for lift coefficients above 0.4. This flap schedule and the drag-due-to-lift data shown in figure 22 were used to develop the curve for

the performance summary representing conventional attached-flow leading-edge flaps.

A comparison of the aerodynamic performance of the vortex-flap wing and the attached-flow flap wing can be made from the data which are summarized in figure 23. In this figure, the aerodynamic performance is expressed as a percent of full, theoretical, leading-edge thrust and is presented as a function of lift coefficient.

For reference purposes, a practical-goal curve was established from experimental data measured on several twisted and cambered wings where each wing camber was optimized for a specific lift coefficient. For example, the data used to generate the portion of the practical-goal curve for lift coefficients from 0.0 to 0.2 were taken from the cruise cambered-wing designs reported in reference 41, and the data used to establish the performance level for the 0.4 value of lift coefficient were taken from the high-lift wing designs reported in references 42 and 43.

The information contained in figure 23 represents the state of the art in experimentally measured supersonic aerodynamic performance. At low levels of lift ($C_L \approx 0.1$), the results indicate that the practical goal of near 100-percent thrust has been obtained with both traditional leading-edge flaps and vortex leading-edge flaps. However, at high-lift conditions ($C_L \approx 0.4$), the practical goal, which is reduced to approximately 60 percent thrust, has not been obtained by either of the flap concepts. At this high-lift condition, the traditional leading-edge flap produces less than 25-percent thrust and the data of reference 40 indicate that this is probably the best that can be obtained using the attached-flow flap concept. However, the conical vortex flap produces approximately 40-percent thrust and it is anticipated that the use of other nonconical flap geometries along with eliminating the hinge-line separation would increase the performance considerably.

CONCLUDING REMARKS

This paper presents an overview of a research program directed at the study of wing leading-edge vortices at supersonic speeds. The studies include both experimental and theoretical investigations and focus primarily on determining planform, thickness and camber effects for delta wings. The effects of planform and leading-edge camber have been experimentally determined, and an experimental study to identify thickness effects has been initiated. Theoretical studies have shown that a modified linearized-theory method, which was capable of predicting the planform effects for flat wings, was not adequate for predicting leading-edge camber effects. Preliminary results obtained with an Euler code have been shown to contain the correct primary-vortex characteristics for delta wings of various planforms and with various amounts of leading-edge camber.

In a summary of measured aerodynamic performance for high-lift conditions, wings with leading-edge vortex flaps were shown to have a considerably higher level of performance (40-percent thrust) than wings employing conventional attached-flow leading-edge flaps (25-percent thrust). However, the performance levels achieved with vortex flaps were considerably less than the performance levels experimentally established as a practical goal (60 percent thrust).

ACKNOWLEDGMENT

The authors wish to thank Dr. Earll M. Murman and Mr. Kenneth G. Powell of the Massachusetts Institute of Technology for providing the Euler solution results presented in this paper.

REFERENCES

1. Carlson, H. W.; and Middleton, W. D.: A Numerical Method for the Design of Camber Surfaces of Supersonic Wings with Arbitrary Planforms. NASA TN D-2341, 1964.

2. Carlson, H. W.; and Miller, D. S.: Numerical Methods for the Design and Analysis of Wings at Supersonic Speeds. NASA TN D-7713, 1974.

3. Mack, R. J.: A Numerical Method for Evaluation and Utilization of Supersonic Nacelle-Wing Interference. NASA TN D-5057, 1969.

4. Kulfan, R. M.; and Sigallo, A.: Real Flow Limitations in Supersonic Airplane Design. AIAA-78-147, Jan. 1978.

5. Carlson, H. W.; and Miller, D. S.: The Influence of Leading-Edge Thrust on Twisted and Cambered Wing Design for Supersonic Cruise. AIAA-81-1656, Aug. 1981.

6. Carlson, H. W.: Aerodynamic Characteristics at Mach Number 2.05 of a Series of Highly-Swept Arrow Wings Employing Various Degrees of Twist and Camber. NASA TM X-332, 1960.

7. Morris, O. A.; and Fournier, R. H.: Aerodynamic Characteristics at Mach Numbers 2.30, 2.60, and 2.96 of a Supersonic Transport Model Having a Fixed, Warped Wing. NASA TM X-1115, 1965.

8. Miller, D. S.; and Schemensky, R. T.: Design Study Results of a Supersonic Cruise Fighter Wing. AIAA-79-0062, Jan. 1979.

9. Mason, W. H.; and Miller, D. S.: Controlled Supercritical Crossflow on Supersonic Wings - An Experimental Validation. AIAA-80-1421, July 1980.

10. Mason, W. H.; Miller, D. S.; Pittman, J. L.; and Siclari, M. J.: A Supersonic Wing Designed for Nonlinear Attached Flow. AIAA-83-0425, Jan. 1983.

11. Miller, D. S.; Pittman, J. L.; and Wood, R. M.: An Overview of Two Non-Linear Supersonic Wing-Design Studies. AIAA-83-0182, Jan. 1983.

12. Lambourne, N. C.; and Bryer, D. W.: Some Measurements in the Vortex Flow Generated by a Sharp Leading Edge Having 65 Degrees Sweep. C.P. No. 447, British A.R.C., 1960.

13. Squire, L. C.: Camber Effects on the Nonlinear Lift of Slender Wings with Sharp Leading Edges. C.P. No. 924, British A.R.C, 1967.

14. Matoi, T. K.: On the Development of a Unified Theory for Vortex-Flow Phenomena for Aeronautical Applications. Contract No. N00014-57-A-0204-0085, MIT, April 1975. (Available from DTIC as AD-A012-339.)

15. Kulfan, R. M.: Wing Airfoil Shape Effects on the Development of Leading-Edge Vortices. AIAA Paper 79-1675, 1979.

16. Manro, M. E.: Transonic Pressure Measurements and Comparison of Theory to Experiment for Three Arrow-Wing Configurations. Vol. I: Experimental Data Report-Basic Data and Effect of Wing Shape. NASA CR-165701, 1981.

17. Rao, D. M.: Leading-Edge Vortex Flap Experiments on a 74-Deg Delta Wing. NASA CR-159161, 1979.

18. Rao, D. M.: Leading-Edge Vortex Flaps for Enhanced Subsonic Aerodynamics of Slender Wings. ICAS 80-13.5, 1980.

19. Smith, C. W.; Campbell, J. F.; and Huffman, J. K.: Experimental Results of a Leading-Edge Vortex Flap on a Highly Swept Cranked Wing. Tactical Aircraft Research and Technology. NASA CP-2162, 1980.

20. Rao, D. M.; and Johnson, T. D.: Investigation of Delta Wing Leading-Edge Devices. J. Aircraft, vol. 18, no. 3, March 1981, pp. 161-167.

21. Rao, D. M.: Segmented Vortex Flaps. AIAA-83-0424, 1983.

22. Johnston, F. T.; Lu, P.; Tinoco, E. N.; and Epton, M. A.: An Improved Panel Method for the Solution of Three-Dimensional Leading-Edge Vortex Flows. Volume I. - Theory Document. NASA CR-3278, 1980.

23. Lan, C. E.; and Chang, J. F.: VORCAM - A Computer Program for Calculating Vortex Lift Effect of Cambered Wings by the Suction Analogy. NASA CR-165800, 1981.

24. Lamar, J. E.; and Herbert, H. E.: Production Version of the Extended NASA-Langley Vortex Lattice FORTRAN Computer Program - Volume I - User's Guide. NASA TM-83303, 1982.

25. Lamar, J. E.; and Campbell, J. F.: Recent Studies at NASA-Langley of Vortical Flows Interacting with Neighboring Surfaces. Aerodynamics of Vortical Type Flows in Three Dimensions, AGARD-CP-342, July 1983.

26. Miller, D. S.; and Wood, R. M.: Lee-Side Flow Over Delta Wings at Supersonic Speeds. NASA TP-2430, 1985.

27. Stanbrook A.; and Squire, L. C.: Possible Types of Flow at Swept Leading Edges. Aeron. Quarterly, vol. XV, Feb. 1964.

28. Ganzer, W.; Hoder, H.; and Szodruch, J.: On the Aerodynamics of Hypersonic Cruise Vehicles of Off-Design Conditions. Proceedings of the XI Congress of the ICAS, Lisbon, Portugal, vol. I., Sept. 10-16, 1978, p. 152-161.

29. Szodruch, J. G.; and Peake, D. J.: Leeward Flow Over Delta Wings at Supersonic Speeds. NASA TM-81187, 1980.

30. Rizzi, A.; Eriksson, L. E.; Schmidt, W.; and Hitzel, S. M.: Simulating Vortex Flows Around Wings. Aerodynamics of Vortical Type Flows in Three Dimensions, AGARD Conference Preprint N. 342, 1983.

31. Carlson, H. W.; and Mack, R. J.: Estimation of Wing Nonlinear Aerodynamic Characteristics at Supersonic Speeds. NASA TP-1718, 1980.

32. Polhamus, E. C.: A Concept of the Vortex Lift of Sharp-Edged Delta Wings Based on a Leading-Edge Suction Analogy. NASA TN D-3767, 1976.

33. Igglesden, M. S.: Wind Tunnel Measurements of the Lift-Dependent Drag of Thin Conically Cambered Slender Delta Wings at Mach Numbers 1.4 and 1.8. Tech. Note No. Aero. 2677, British A.R.C., 1960.

34. Michael, W. H., Jr.: Flow Studies on Drooped-Leading-Edge Delta Wings at Supersonic Speeds. NACA TN-3614, 1956.

35. Newsome, R. W.; and Thomas, J. L.: Computation of Leading-Edge Vortex Flows. Presented at the Vortex Flow Aerodynamics Conference, NASA Langley Research Center, October 8-10, 1985.

36. Perez, E.: Computation of Conical Flows with Leading Edge Vortices. S.M. Thesis, MIT, 1984.

37. Powell, K. G.; Perez, E. S.; Murman, E. M.; and Baron, J. R.: Total Pressure Loss in Vortical Solutions of the Conical Euler Equations. AIAA Paper 85-1701, July 1985.

38. Murman, E. M.; Rizzi, A.; and Powell, K.: High Resolution Solutions of the Euler Equations for Vortex Flows. Progress & Supercomputing in Computational Fluid Dynamics, Birkhauser-Boston, Inc., 1985.

39. Jameson, A.; Schmidt, W.; and Turkel, E.: Numerical Solution of the Euler Equations by Finite Volume Method Using Runge-Kutta Time-Stepping Schemes. AIAA-81-1259, June 1981.

40. Covell, P. F.; Miller, D. S.; and Wood, R. M.: An Evaluation of Leading-Edge Flap Performance on Delta and Double Delta Wings at Supersonic Speeds. AIAA-86-0315, 1986.

41. Wood, R. M.; Miller, D. S.; Raney, D. L.; and Roesch, M. T.: A Low-Lift Wing Camber Design Approach for Fighter Aircraft. NASA TP-2465, 1985.

42. Miller, D. S.; Landrum, E. J.; Townsend, J. C.; and Mason, W. H.: Pressure and Force Data for a Flat Wing and a Warped Conical Wing Having a Shockless Recompression at Mach 1.62. NASA TP-1759, 1981.

43. Pittman, J. L.; Miller, D. S.; and Mason, W. H.: Supersonic, Nonlinear Attached-Flow Wing Design for High Lift with Experimental Validation. NASA TP-2336, 1984.

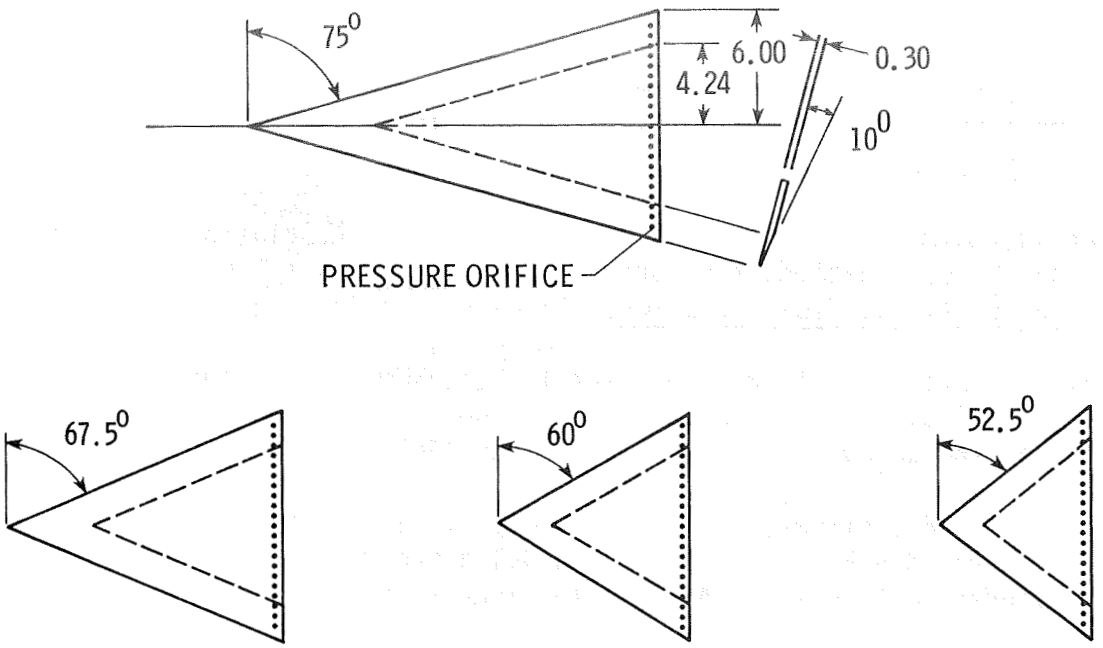

Figure 1. Planforms of flat delta-wing models.

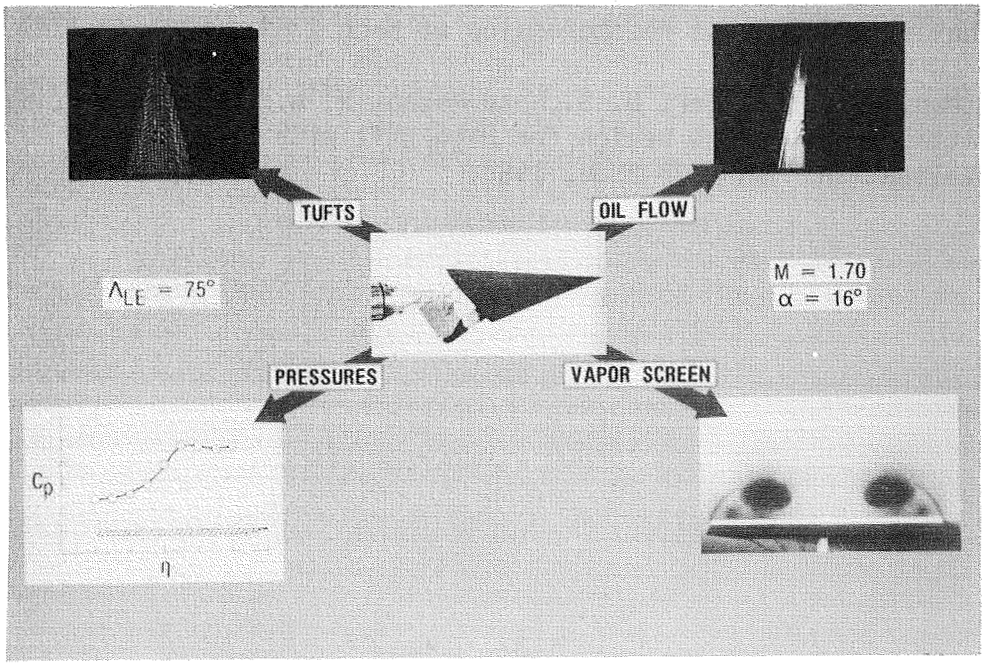

Figure 2. Types of experimental data.

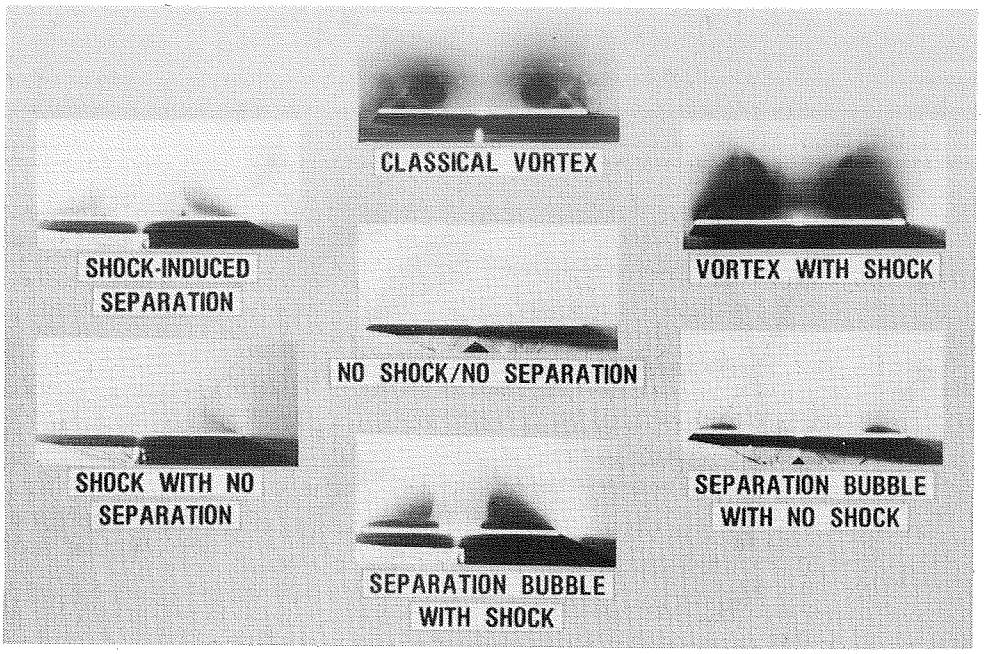

Figure 3. Flow classifications.

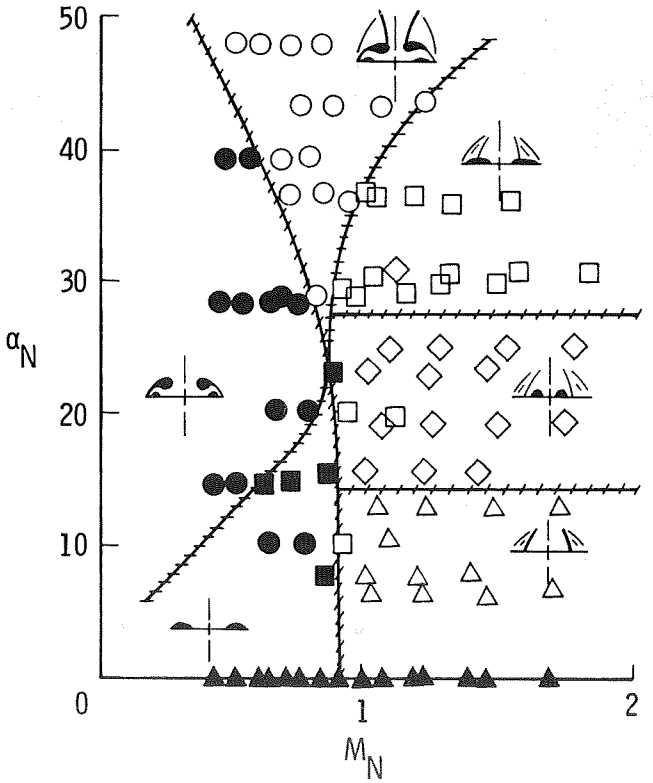

Figure 4. Classification of test data.

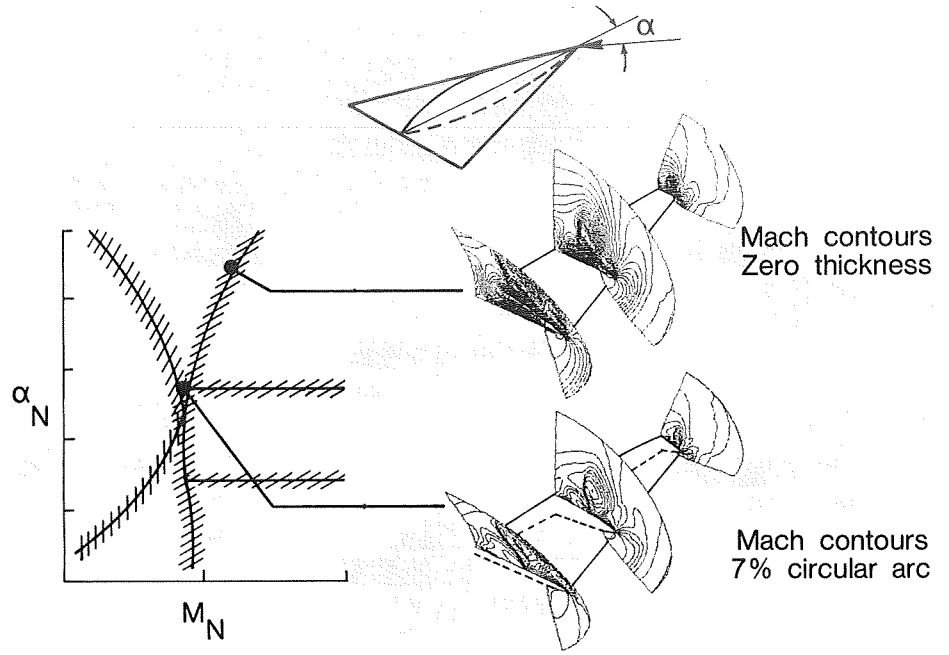

Figure 5. Estimated thickness effects.

Experimental flow visualization

$\Lambda = 52.5° - 75°$

$M = 1.5 - 2.8$

$\alpha = 0° - 20°$

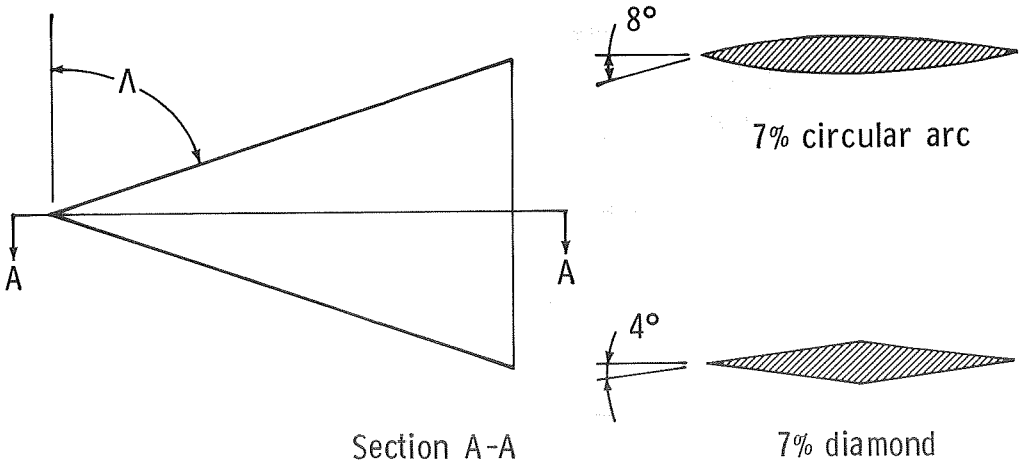

Figure 6. Elements of thickness effects study.

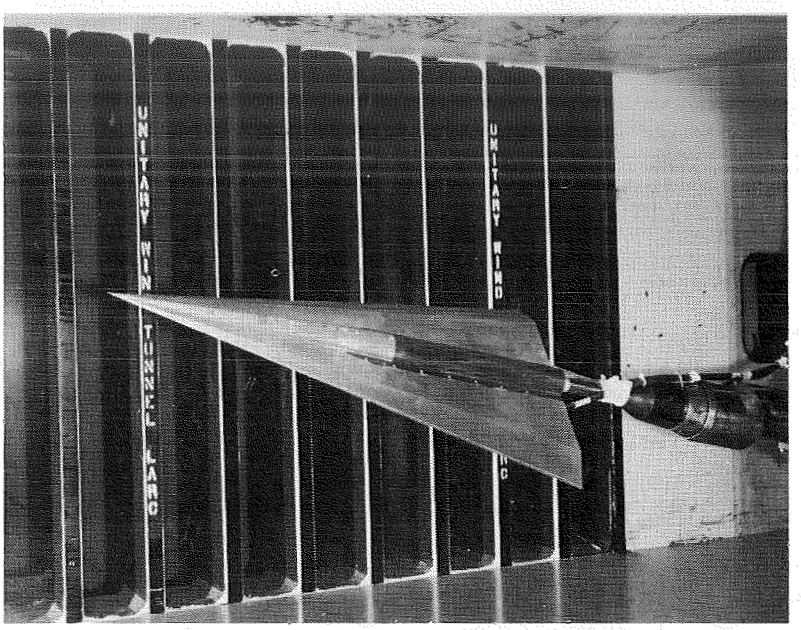

Figure 7. Photograph of $\Lambda = 75°$ conical wing-flap model.

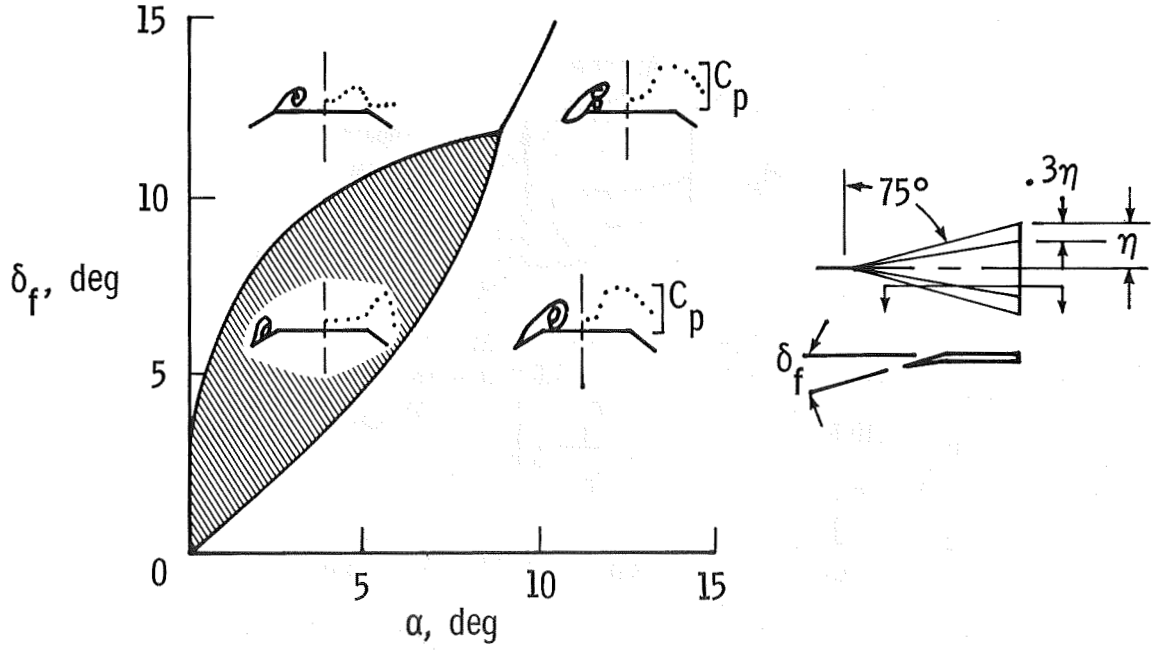

Figure 8. Typical wing-flap leeside flow characteristics.

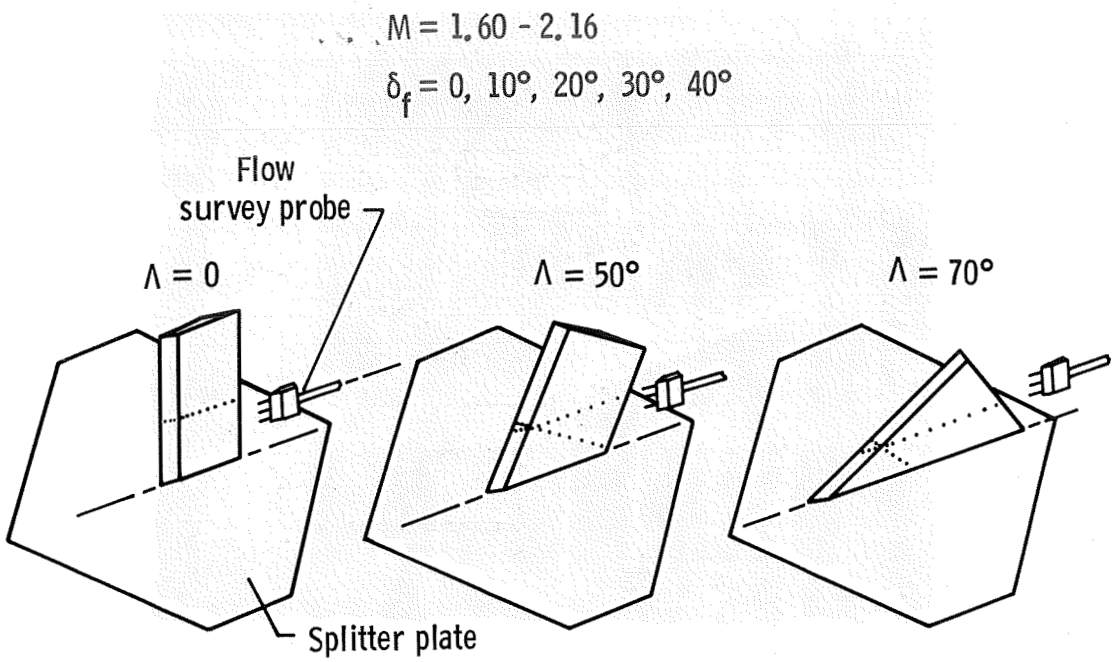

Figure 9. Elements of hinge-line study.

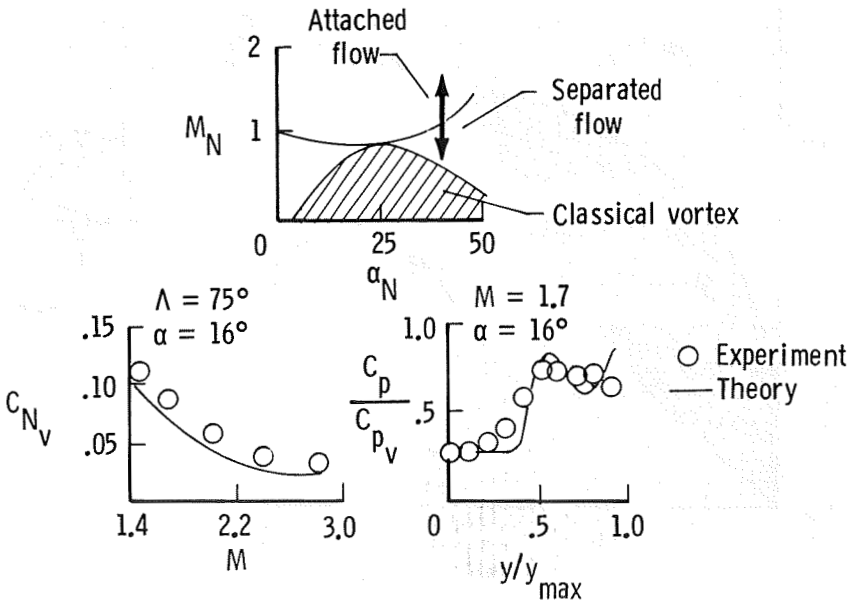

Figure 10. Modified linear-theory predictions for uncambered delta wing.

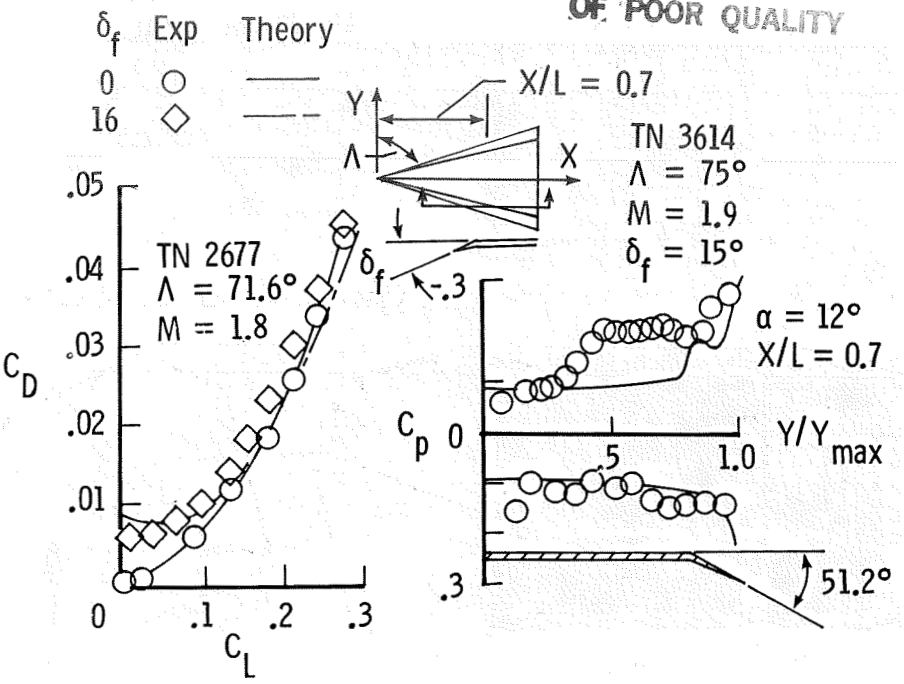

Figure 11. Modifed linear-theory predictions for delta wing with leading-edge flap.

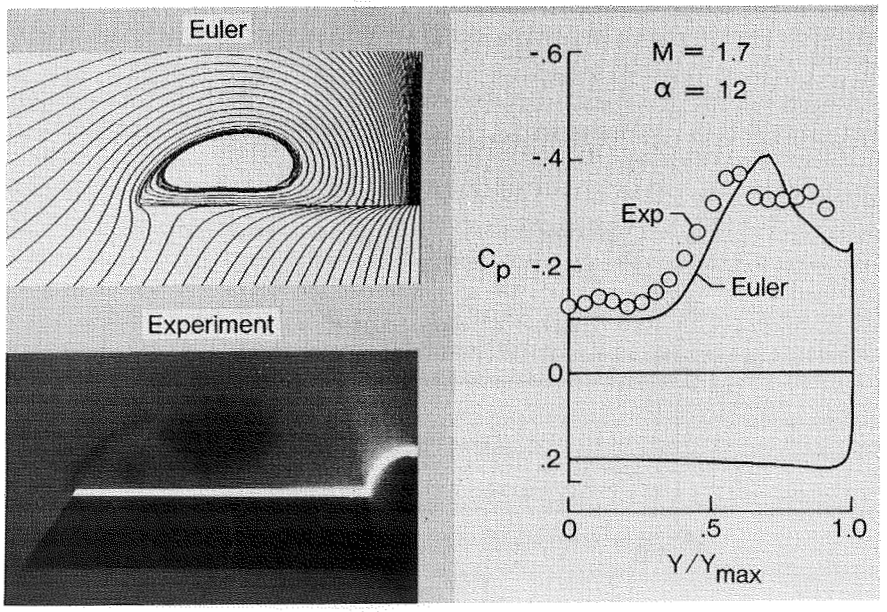

Figure 12. Experimental and Euler code results for flat delta wing at M = 1.7, α = 12°, β = 0°.

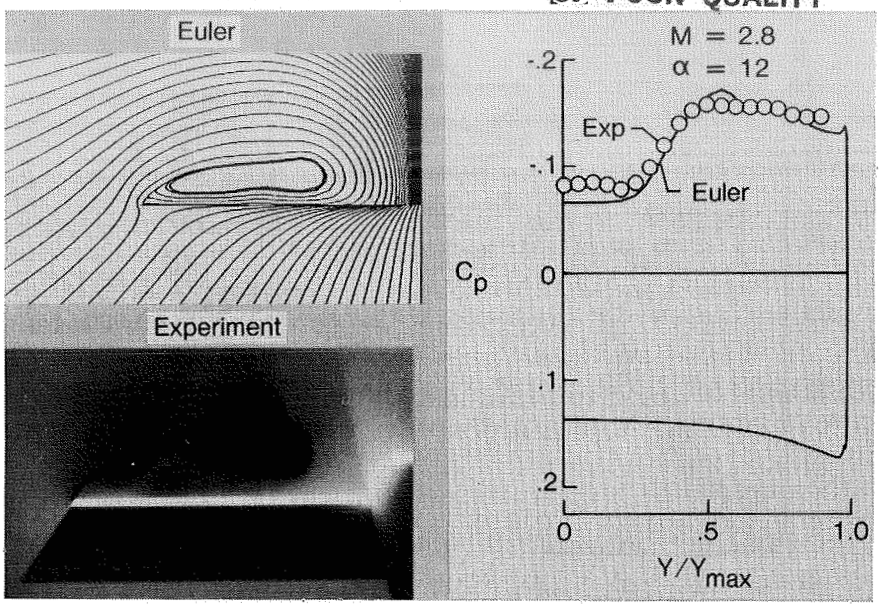

Figure 13. Experimental and Euler code results for flat delta wing at M = 2.8, $\alpha = 12°$, $\beta = 0°$.

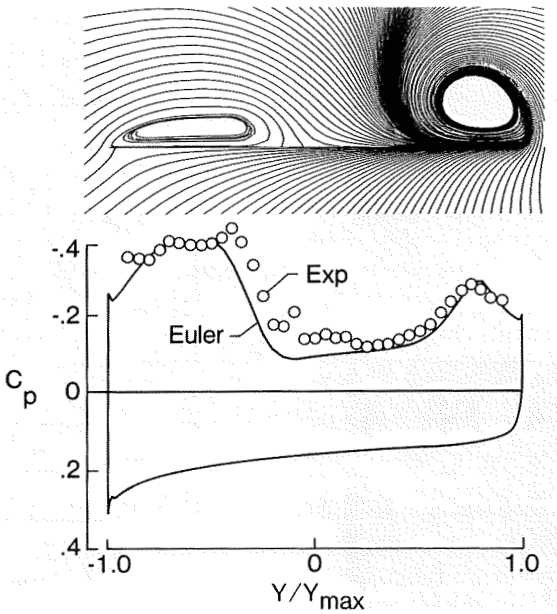

Figure 14. Experimental and Euler code results for flat delta wing at M = 1.7, $\alpha = 12°$, $\beta = 8°$.

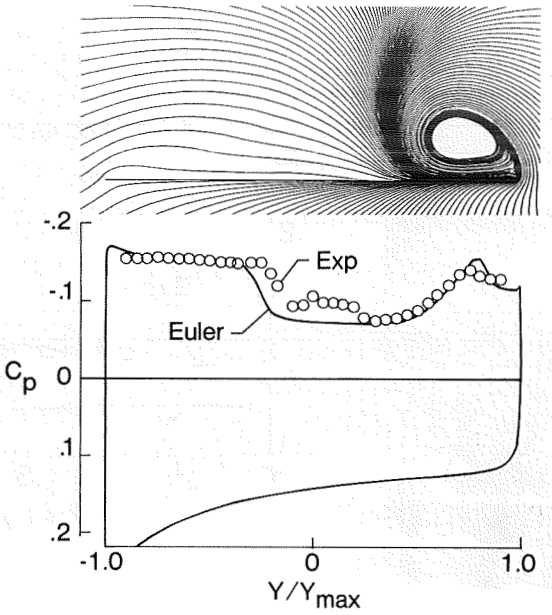

Figure 15. Experimental and Euler code results for flat delta wing at M = 2.8, α = 12°, β = 8°.

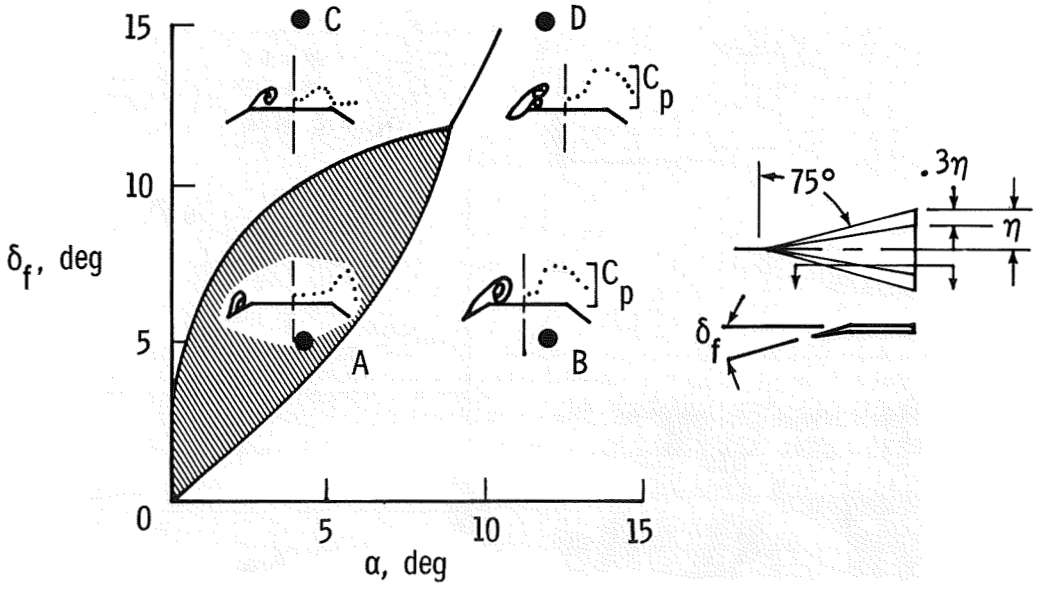

Figure 16. Illustration of the four wing flap conditions subjected to Euler code analysis.

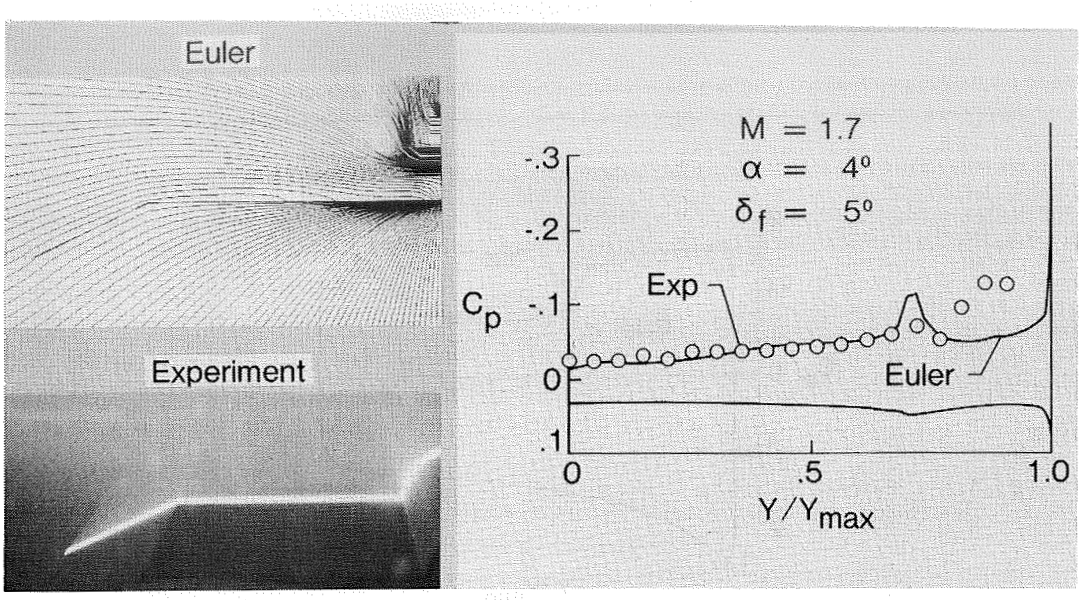

Figure 17. Experimental and Euler code results for wing flap at M = 1.7, $\alpha = 4°$, $\delta_f = 5°$.

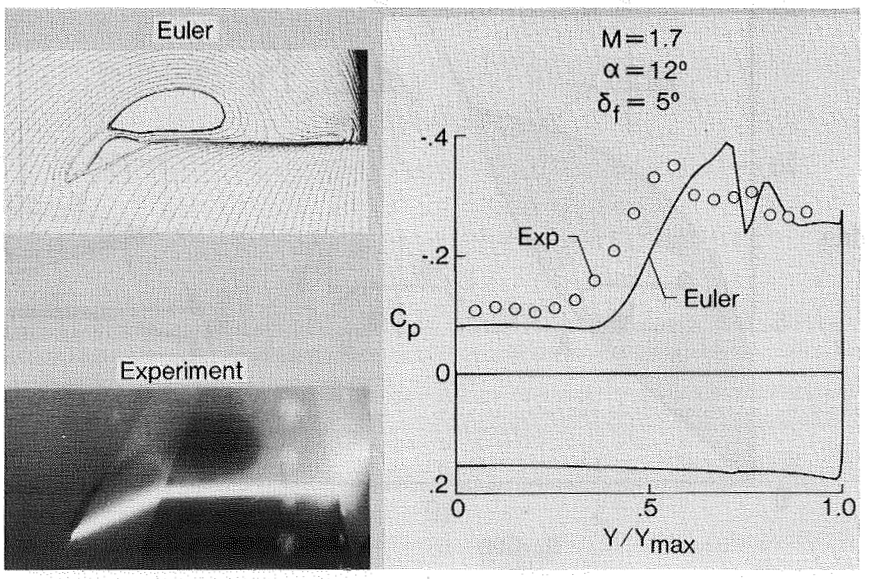

Figure 18. Experimental and Euler code results for wing flap at M = 1.7, $\alpha = 12°$, $\delta_f = 5°$.

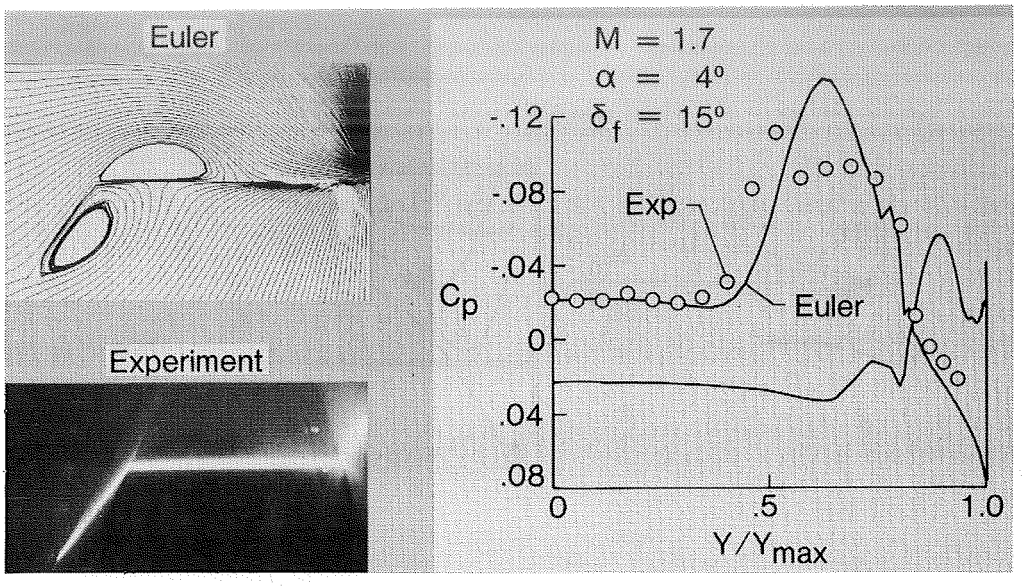

Figure 19. Experimental and Euler code results for wing flap at M = 1.7, $\alpha = 4°$, $\delta_f = 15°$.

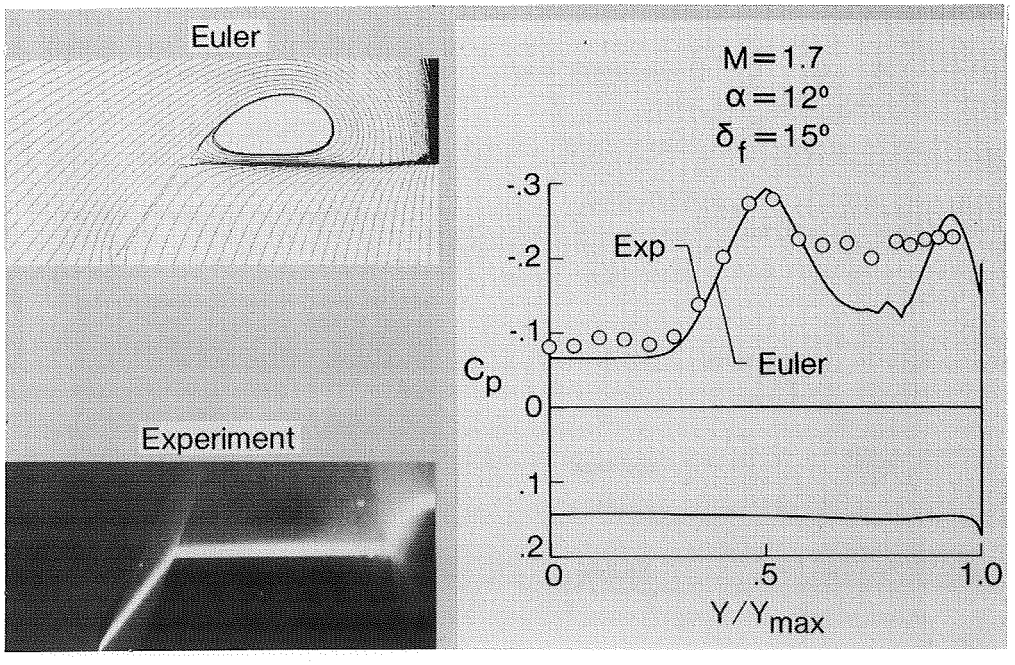

Figure 20. Experimental and Euler code results for wing flap at M = 1.7, $\alpha = 12°$, $\delta_f = 15°$.

C-5

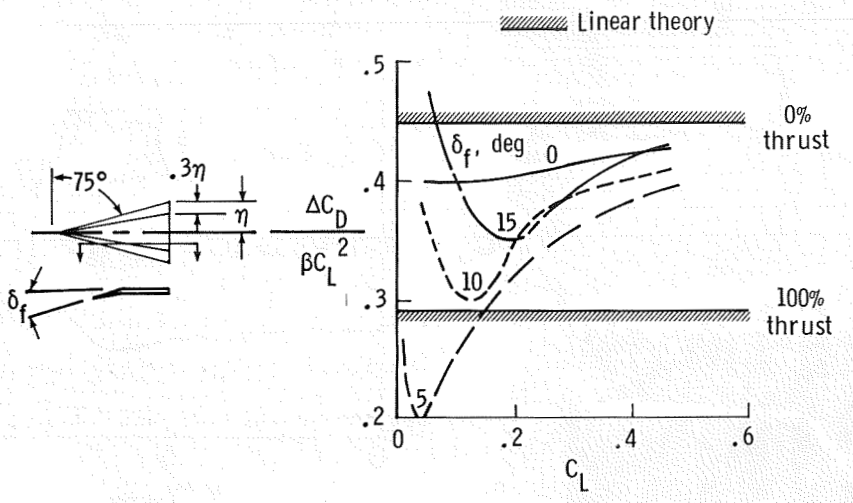

Figure 21. Experimental drag-due-to-lift factor for conical wing flap.

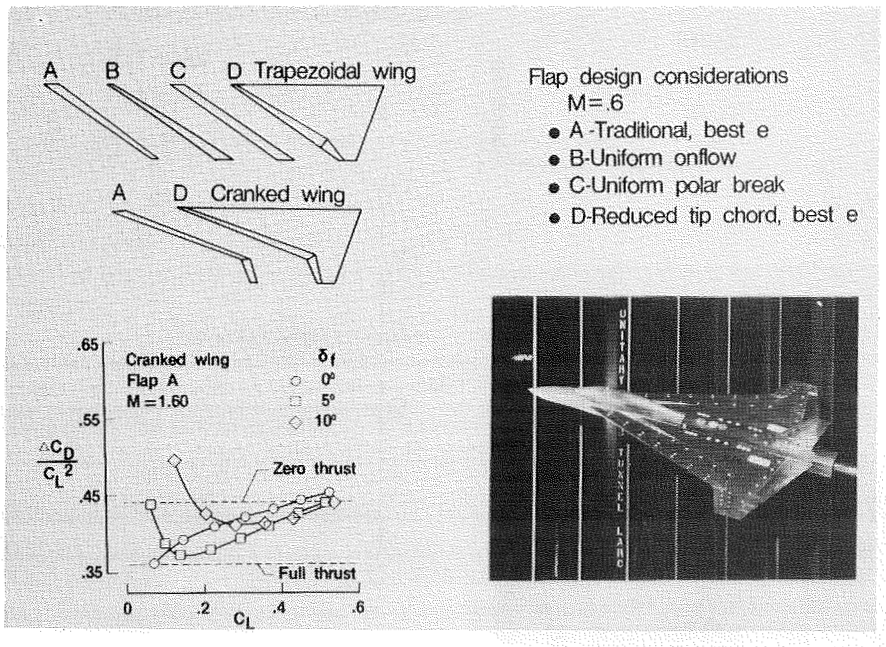

Figure 22. Elements of conventional leading-edge flap study.

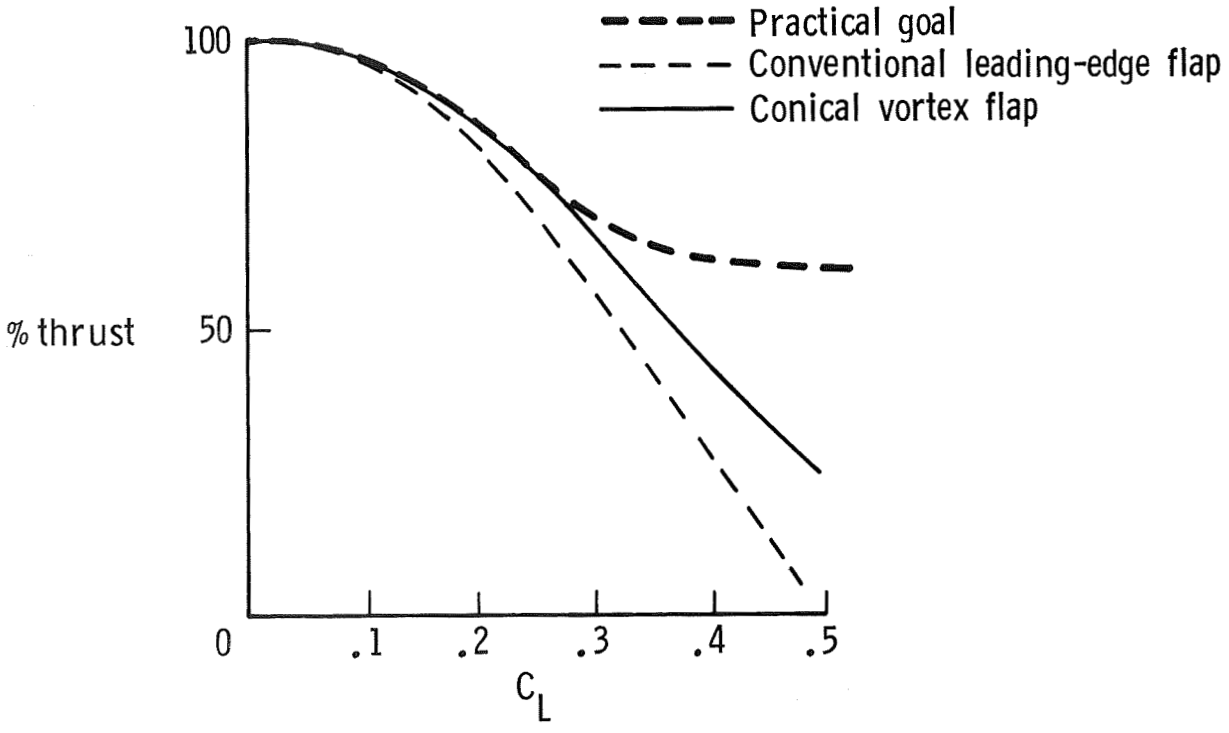

Figure 23. Supersonic performance summary.